# Compressive Sensing based ISAR Imaging from Incomplete Data

S. Tomei[1,2], A. Bacci[1,2], E. Giusti [1,2], M. Martorella [1,2], F. Berizzi [1,2]

[1] *Department of Information Engineering, University of Pisa, Italy*

[2] *CNIT Radar and Surveillance System (RaSS), Pisa, Italy*

**Abstract**

The applicability of Compressive Sensing (CS) to radar imaging has been recently proven and its capability to construct reliable radar images from a limited set of measurements demonstrated. In this paper, a CS-based ISAR imaging method is proposed. The proposed method is tested for application such as image reconstruction from compressed data, resolution enhancement and image reconstruction from gapped data. The effectiveness of the proposed method is demonstrated on real datasets and the performance evaluated by means of image contrast.

**Index Terms**

TBD

## I. INTRODUCTION

ISAR imaging is a widely exploited technique used to obtain high resolution images of moving targets by means of Fourier based imaging methods [31][5]. In particular, the transmission of large bandwidth signals and the coherent integration of the received echoes from different aspect angles are the key aspects to obtain images with fine resolution both in range and cross range. By the way, real data can present missing samples both in the frequency and slow time domain because of system malfunctioning or data compression for storage resource issues. In this scenario, images obtained with Fourier based methods, such as the Range Doppler (RD) algorithm [5], can be distorted because of the lack of data or can present a coarse resolution. Recent results in signal processing have demonstrated the ability of Compressive Sensing (CS)

to reconstruct a sparse or compressible signal from a limited number of measurements with a high probability by solving an optimization problem [7]. Such a technique has been successfully applied for data storage reduction in medical imaging [17] and radar imaging applications [2] among others. One of the key aspect for the successful application of CS is that the signal must be sparse, which means that it can be represented by few non-zero samples in a suitable orthonormal basis. Different basis can be identified which support different sparsity index such as that proposed in [8]. Specifically, the applicability of CS to the radar imaging problem has been justified by observing that at high frequencies a radar signal is sparse in the image domain, i.e. when represented in the 2D Fourier basis, since it can be approximated by the superimposition of few prominent scatterer responses in the radar image plane with respect to the pixels in the image. CS reconstruction capabilities has been tested for a number of radar applications, such as Synthetic Aperture Radar Imaging (SAR) and Inverse Synthetic Radar Imaging (ISAR) [26], ground penetrating radars [14], Multiple Input Multiple Output (MIMO) radar [33][1] and 3D ISAR imaging [25]. Specifically, three different applications of CS to the ISAR imaging problem has been described in literature. First of all, CS can be applied for the reconstruction of ISAR images from data with random missing samples. For example, in [30] and [29], CS has been suggested as an effective ISAR image reconstruction tool in the case of data with missing samples in the slow time and in the frequency domain, respectively. In addition, given the CS capability of reconstructing images from undersampled data, the sampling constraints related to Nyquist's sampling theorem can be overcame, as demonstrated in [3]. CS for data storage reduction has been suggested also in [6], [37] and [16]. In [13], CS has been suggested as an effective reconstruction tool to recover a signal from its principal component extracted via Principal Component Analysis (PCA) in order to reduce the clutter effects and enhance the target return extraction. In this framework, the advantages of CS can be mainly associated with the capability of obtaining good quality images from a limited number of measurements thus reducing the amount of data to be stored and processed.

On the other hand, CS processing can be successfully applied to achieve resolution enhancement in both delay time/ range and Doppler/ cross-range domain, as suggested in [36]. Specifically, CS can be applied to reconstruct the image from data considering a larger data support in the frequency/slow-time domain, thus enhancing the resolution in range and cross-range [12].

Finally, the CS can be used to process data that are not complete in one domain, presenting large

portions of missing samples. Data can be incomplete, or *gapped*, in the slow time domain such as data acquired by a multiple target tracking radar which collects data from different targets in different and not adjacent slow time intervals, as shown in [34] and [38]. On the other hand, data can be gapped in the frequency domain such as the signal obtained by transmitting over different non-adjacent channels within a large bandwidth [35]. This latter case coincides with the case of passive radars which exploit the DVB-T signals transmitted for broadcast TV services. In this paper a common framework for the application of CS to ISAR imaging is provided. Specifically, a CS-based ISAR imaging method is proposed for all the above mentioned applications. The effectiveness of such a method and its performances against different SNR values will be proven by using the image contrast as image quality criteria on both simulated and real data. It is worth saying that different quality criteria for CS-based ISAR imaging algorithms can been identified, such as the one proposed in [10]. The reminder of the paper is organized as follows. Section II presents the ISAR signal model in a CS framework and the proposed CS-based imaging algorithm. Section III shows the results of the proposed CS based imaging algorithm in different applications using simulated data while Section V demonstrate the effectiveness of the proposed method on real data. Final comments are summarized in Section VI.

## II. Signal Model

Let consider the geometry in Fig.1 where $T_z(z_1, z_2, z_3)$ is a Cartesian reference system embedded on the target, $T_\xi(\xi_1, \xi_2, \xi_3)$ is a Cartesian reference system centred on the transmitter, $R_{TxTg}$ ,$R_{RxTg}$ ,$R_{TxRx}$ represent the transmitter-target, and receiver-target, transmitter-receiver distances, $\beta$ is the bistatic angle and $\mathbf{i}_{LoSBi}$ is the unit vector identifying the bisector of the bistatic angle [12].

It is worth pointing out that the bistatic geometry in Fig.1 can be used to model the received signal in both active and passive radar systems, and both monostatic and bistatic configurations.

It is well known that under the *stop & go* assumption, the target motion can be split into two components: a translational motion denoted by $R_0(t)$, and a rotational component which can be described by means of the total angular rotation vector, $\mathbf{\Omega}_T(n)$, while the motion component which contributes to the synthetic aperture formation is denoted by the effective rotation angle $\mathbf{\Omega}_{eff}(n)$. It is worth pointing out that the translational component is assumed to be perfectly compensated by means of autofocusing techniques [11][19] before the application of CS-based
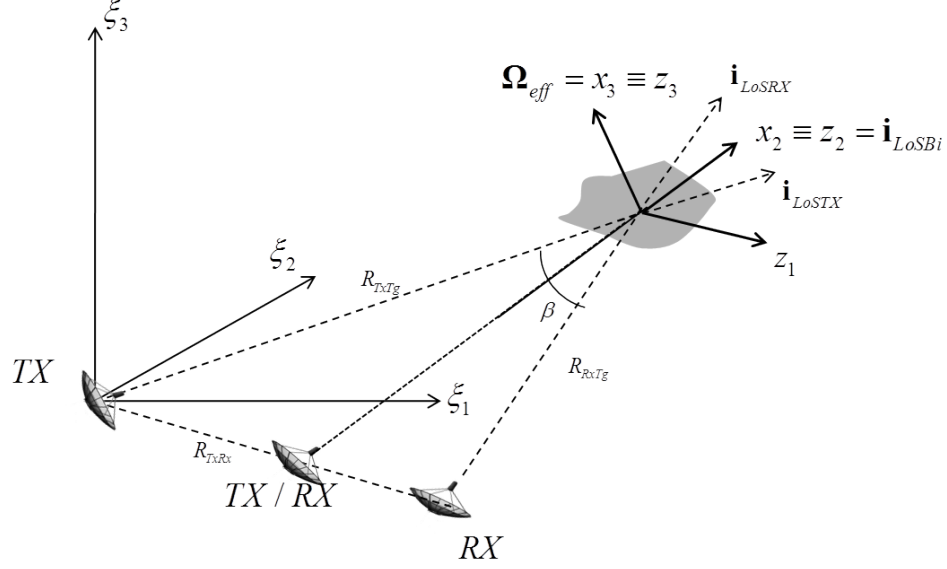
Figure 1. Bistatic geometry representation

imaging algorithm. However, it is worth remarking that different signal models have been proposed in literature which include the motion compensation step while solving the optimization problem related to CS, such as the one proposed in [27]. In addition, it is assumed that the target is stationary during the transmission and reception of a sweep or a pulse, thus the slow time can be considered a discrete variable, which will be denoted by $n$. The received signal can be defined as

$$s_R(t,n) = \int_V \gamma'(\mathbf{z}) s_T(t - \tau(\mathbf{z},n), n) h(n) \, d\mathbf{z} \qquad (1)$$

where $s_T(t,n)$ is the transmitted signal within the $n^{th}$ sweep, $t$ denotes the fast time, $n = 1, .., N$, $N$ is the number of transmitted sweeps, $\tau(\mathbf{z},n) = \frac{R_{TxTg}(\mathbf{z},n) + R_{RxTg}(\mathbf{z},n)}{c}$ represents the delay-time of a point on the target with coordinates $\mathbf{z}$ in the Cartesian reference system $T_z$, at the $n^{th}$ sweep, $c$ is the speed of the light in a vacuum, $h(n)$ is the signal support in the slow time domain and $\gamma'(\mathbf{z})$ is the target reflectivity function defined within the volume $V$ occupied by the target. At the output of the matched filter, after Fourier transforming along the time domain, the baseband signal in the frequency/slow-time domain can be expressed as

$$S_R(f, n) = W(f, n) \int\limits_V \gamma'(\mathbf{z}) e^{-j2\pi f \tau(\mathbf{z}, n)} d\mathbf{z} \tag{2}$$

where $f$ denotes the frequency which is the Fourier transform variable of the fast time $t$. A special attention should be given to the signal support $W(f, n)$ which defines the region occupied by the signal $S_R(f, n)$ in the Fourier domain. At the output of the matched filter, $W(f, n)$ is given by

$$W(f, n) = |S_T(f, n)|^2 h(n) \tag{3}$$

where $h(n) = u(n) - u(n-N)$ and $u(n)$ is the unit step discrete function. When the transmitted signal is unchanged over adjacent sweeps, which is usually the case for active radar systems, Eq.(3) can be rewritten as $W(f, n) = |S_T(f)|^2 h(n)$ .

In the case of passive radars, according to the CAF (Cross Ambiguity Function) batches algorithm proposed in [23], in order to form the RD image, both the transmitted and the received signal are split into $N$ batches of fixed temporal length, so that each batch is associated to a different sweep. Since the broadcast signal is content dependent, the transmitted signal can change from batch to batch, therefore Eq.(3) is appropriate for the passive case as well.

Assume that the effective rotation angle of the target is constant within the observation time, $\Omega_{eff}(n) \approx \Omega_{eff}$, and assume that the Cartesian reference system $T_z$ is oriented so that $z_3$ is parallel to $\Omega_{eff}$. In this case, under the straight iso-range approximation, the signal after motion compensation can be rewritten as [20]

$$S(f, n) = W(f, n) \int\limits_{z_1} \int\limits_{z_2} \gamma(z_1, z_2) e^{-j \frac{4\pi f}{c} \cos\left(\frac{\beta(n)}{2}\right)(z_1 \cos(\Omega_{eff} n) + z_2 \sin(\Omega_{eff} n))} dz_1 dz_2 \tag{4}$$

where $\gamma(z_1, z_2) = \int\limits_{z_3} \gamma'(\mathbf{z}) dz_3$ is the target reflectivity function projection onto the image plane.

Suppose that the target consists of $K$ pointlike scatterers and that the interactions among scatterers can be neglected, so that its reflectivity function becomes

$$\gamma(z_1, z_2) = \sum_{k=1}^{K} \sigma_k \delta\left(z_1 - z_1^{(k)}, z_2 - z_2^{(k)}\right) \tag{5}$$

where $\sigma_k$ is the complex amplitude of the $k^{th}$ scatterer.

Under this hypothesis and assuming that the bistatic angle variation is relatively small within the observation time, $\beta(n) \approx \beta(0) = \beta_0$ , Eq.(4) can be rewritten as

$$S(f,n) = W(f,n) \sum_{k=1}^{K} \sigma_k e^{-j\frac{4\pi f}{c} k_0(z_1^{(k)} \cos(\Omega_{eff}n) + z_2^{(k)} \sin(\Omega_{eff}n))} \tag{6}$$

where $k_0 = cos\left(\frac{\beta_0}{2}\right)$.

Changes in the bistatic angle affect the Point Spread Function (PSF) of the system and can cause defocusing effects as demonstrated in [20].

By defyining the spatial frequencies as

$$\begin{aligned}
Z_1(f,n) &= \frac{2fk_0 cos(\Omega_{eff}n)}{c} \\
Z_2(f,n) &= \frac{2fk_0 sin(\Omega_{eff}n)}{c}
\end{aligned} \tag{7}$$

Eq.(6) can be rewritten as

$$\begin{aligned}
S(Z_1, Z_2) &= W(Z_1, Z_2) \sum_{k=1}^{K} \sigma_k e^{-j2\pi\left(z_1^{(k)} Z_1 + z_2^{(k)} Z_2\right)} \\
&= W(Z_1, Z_2)\Gamma(Z_1, Z_2)
\end{aligned} \tag{8}$$

where $\Gamma(Z_1, Z_2) = \sum_{k=1}^{K} \sigma_k e^{-j2\pi\left(z_1^{(k)} Z_1 + z_2^{(k)} Z_2\right)}$ is the Fourier transform of the target reflectivity function $\gamma(z_1, z_2)$.

Eq.(8) clearly shows that the motion compensated signal is related to the Fourier transform of the target reflectivity function. In particular, the inverse Fourier transform of Eq.(8) s given by

$$\begin{aligned}
I(z_1, z_2) &= w(z_1, z_2) \otimes \otimes \gamma(z_1, z_2) \\
&= \sum_{k=1}^{K} \sigma_k w(z_1 - z_1^{(k)}, z_2 - z_2^{(k)})
\end{aligned} \tag{9}$$

where the symbol $\otimes\otimes$ denotes the 2D convolution operator, $w(z_1, z_2)$ is the inverse Fourier transform of $W(Z_1, Z_2)$ and coincides with the PSF of the system in the range/cross-range domain.

It is worth pointing out that the knowledge of the modulus of the effective target rotation vector, $\Omega_{eff}$ , is needed to calculate the inverse Fourier transform. It is usually known in SAR systems where the motion of the platform is known a priori. Conversely, in ISAR systems the target is non-cooperative and, hence, $\Omega_{eff}$ is not known. As a consequence, $\Omega_{eff}$ should be estimated before forming the ISAR image.

Under the hypothesis that the aspect angle variation within the observation time is sufficiently small ($\Delta\theta = \Omega_{eff}T_{obs} << 10$) [5], the spatial frequencies can be approximated as follows:

$$
\begin{aligned}
Z_1(f,n) &\approx \frac{2fk_0}{c} \\
Z_2(f,n) &\approx \frac{2f_0 k_0 \Omega_{eff} n}{c}
\end{aligned}
\tag{10}
$$

This means that the region in the Fourier domain where the signal is defined can be approximated by a rectangular domain. Therefore, the two spatial frequencies can be assumed to be independent of each other and a two-dimensional Fast Fourier Transform (FFT) can be applied to form the ISAR image.

In particular, under the assumption of small aspect angle variation, the received signal after motion compensation can be rewritten as

$$
S(f,n) = W(f,n) \sum_{k=1}^{K} \sigma_k e^{-j\frac{4\pi k_0}{c}\left(f z_1^{(k)} + f_0 z_2^{(k)} \Omega_{eff} n\right)}
\tag{11}
$$

Let the variables $(\tau, \upsilon)$ represent the delay-time and Doppler frequency respectively, which are defined as

$$
\begin{aligned}
\tau &= \frac{2z_1 k_0}{c} \\
\upsilon &= \frac{2f_0 k_0 \Omega_{eff} z_2}{c}
\end{aligned}
\tag{12}
$$

By substituting Eq.(12) into Eq.(11), the motion compensated signal becomes

$$
S(f,n) = CW(f,n) \sum_{k=1}^{K} \sigma_k e^{-j2\pi(f\tau_k + n\upsilon_k)}
\tag{13}
$$

where $C = \frac{c^2}{4f_0 k_0^2 \Omega_{eff}}$.

It is worth noting that the summation in Eq. (13) represents the two-dimensional Fourier series of the target reflectivity function in the delay-time/Doppler domain. Eq. (12) suggests how to scale the ISAR image from delay-time/Doppler domain to range/cross-range domain and vice-versa. The use of Eq.(12) and Eq.(13) allows for an ISAR image to be formed also when $\Omega_{eff}$ remains unknown. Nevertheless, in order to scale the ISAR image using spatial coordinates along the cross-range, $\Omega_{eff}$ must be estimated [18].

In a real scenario, both the variables in the signal domain $(f, n)$ and in the image domain $(\tau, \upsilon)$ are discrete variables. It is therefore appropriate to write the signal in Eq.(13) as a function of discrete variables, defined as follows

$$
\begin{aligned}
f &= f_0 + m\Delta f & m &= 1, ..., M \\
t &= nT_R & n &= 1..., N \\
\upsilon &= p\Delta\upsilon & p &= 1, ..., P \\
\tau &= q\Delta\tau & q &= 1, ..., Q
\end{aligned}
\tag{14}
$$

where $\Delta f$ is the frequency step, $T_R$ is the Pulse Repetition Interval (PRI), $\Delta\upsilon = \frac{1}{NT_R} = \frac{1}{T_{obs}}$ is the Doppler frequency pixel spacing and $\Delta\tau = \frac{1}{Q\Delta f}$ is the delay-time pixel spacing.

It is worth remarking that usually $Q = M$ and $P = N$ and when this holds, $\Delta\nu$ and $\Delta\tau$ coincide with the Doppler and the delay-time resolutions.

By exploiting Eq.(14) the discrete version of the received signal after motion compensation can be written as

$$
S(m, n) = C \cdot W(n, m) \cdot \sum_{k=1}^{K} \sigma_k e^{-j2\pi \frac{mq_k}{Q}} e^{-j2\pi \frac{np_k}{P}}
\tag{15}
$$

where $W(m, n) = (u(n) - u(n - N)) \cdot (u(m) - u(m - M))$ is the signal support in the discrete slow time/frequency domain and $u(.)$ is the unit step discrete function.

Eq. (15) highlights that the received signal after motion compensation is linked to the 2D Fourier transform of the target reflectivity function. Therefore, by using the inverse Fourier transform of Eq. (15), the ISAR image which represents an approximation of the target reflectivity function, can be expressed as

$$
I(q, p) = C \sum_{k=1}^{K} \sigma_k \cdot w(q - q_k, p - p_k)
\tag{16}
$$

For the sake of simplicity, it is possible to write the relation between $S(m,n)$ and $I(q,d)$ in a matricial form. In order to use a notation coherent with all the applications described in this document, the ISAR data after motion compensation, $S(m,n)$, will be identified by the matrix $\overline{\mathbf{S}}_c$, while the ISAR image, $I(q,p)$, will be identified by the matrix $\mathbf{I}$, as follows

$$\overline{\mathbf{S}}_c = \mathbf{\Psi}_x \mathbf{I} \mathbf{\Psi}_y^T \tag{17}$$

where $\mathbf{\Psi}_x \in \mathbb{C}^{M \times Q}$ and $\mathbf{\Psi}_y \in \mathbb{C}^{N \times P}$ are the Fourier dictionaries that perform the range compression and the cross range compression respectively.

The generic element of the Fourier dictionaries is defined as follows

$$\begin{aligned}
[\mathbf{\Psi}_x]_{n,p} &= e^{-j2\pi \frac{np}{P}} \\
[\mathbf{\Psi}_y]_{m,q} &= e^{-j2\pi \frac{mq}{Q}}
\end{aligned} \tag{18}$$

where $\mathbf{\Psi}_x$ and $\mathbf{\Psi}_y$ are defined as *complete Fourier matrices*, in which $P = N$ and $Q = M$.

The signal in Eq.(17) represents the *complete* data from which the ISAR image can be obtained by applying Fourier based methods with a resolution given by the theoretical bounds [4]. In a real scenario, the signal acquired by the system can suffer from data loss due to hardware malfunctioning or compression requirements. In these cases, the acquired signal is assumed to be obtained from the signal in Eq.(17) after a sensing process

$$\begin{aligned}
\mathbf{S} &= \mathbf{\Phi}_x \mathbf{\Psi}_x \mathbf{I} \mathbf{\Psi}_y^T \mathbf{\Phi}_y^T \\
&= \mathbf{\Theta}_x \mathbf{I} \mathbf{\Theta}_y^T
\end{aligned} \tag{19}$$

where $\mathbf{S} \in \mathbb{C}^{M' \times N'}$, $\mathbf{I} \in \mathbb{C}^{M \times N}$. The matrices $\mathbf{\Phi}_x \in \mathbb{C}^{M' \times M}$ and $\mathbf{\Phi}_y \in \mathbb{C}^{N' \times N}$ represent the sensing matrices which performs the random selection of samples in the frequency/slow time domain respectively and $M' < M$ and $N' < N$ are the data dimensions after the sensing operation.

$\mathbf{\Theta}_x$ and $\mathbf{\Theta}_y$ are the undercomplete Fourier matrices which satisfy the RIP property and provide stronger non-coherence than the Gaussian matrix [36]. These matrices are defined by taking into account the indexes of the pulses and frequency bins selected by the sensing process. In particular, the generic element of the these matrices are defined as follows
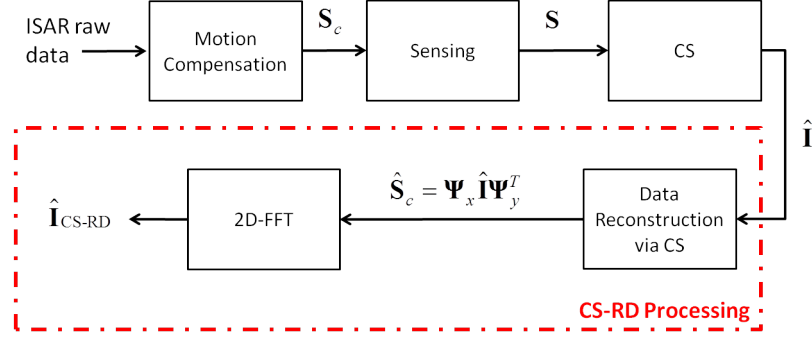
Figure 2. CS image reconstruction block diagram

$$[\boldsymbol{\Theta}_x]_{i,p} = e^{-j2\pi\frac{pn_i}{P}}$$
$$[\boldsymbol{\Theta}_y]_{i,q} = e^{-j2\pi\frac{qm_i}{Q}}$$

$$(20)$$

where $\{n_i\}_{i=1}^{N'}$ are the pulse indexes, $\{m_j\}_{j=1}^{M'}$ are the frequency bin indexes while $p$ and $q$ are defined in Eq.(14).

According to the CS formulation, the image reconstruction process in case of noise is based on a minimization problem, given by [7]

$$\hat{\mathbf{I}} = \min_{\mathbf{I}}\|\mathbf{I}\|_{\ell_0} \quad s.t. \quad \|\mathbf{S} - \boldsymbol{\Theta}_{\mathbf{x}}\mathbf{I}\boldsymbol{\Theta}_{\mathbf{y}}^T\|_F^2 \le \epsilon \tag{21}$$

where $\|\cdot\|_F$ denotes the Frobenius norm and $\|\cdot\|_{\ell_0}$ denotes the $\ell_0$-norm. The minimization algorithm in Eq.(21) can be solved via 2D-SL0 algorithm [9].

It is worth pointing out that the image at the output of the CS reconstruction algorithm cannot be directly compared with the image at the output of the RD algorithm because there is no relationship between the pixel size and the spatial resolution of the image in the Rayleigh sense [5]. For this reason, a raw data is reconstructed from the CS image, as shown in Fig.2, by means of the Fourier dictionaries as

$$\hat{\mathbf{S}} = \boldsymbol{\Psi}_x\hat{\mathbf{I}}\boldsymbol{\Psi}_y^T \tag{22}$$

At this point, an ISAR image can be obtained by means of the conventional RD algorithm applied to the reconstructed data and can be fairly compared with the image obtained via RD algorithm applied to the original data.

## III. CS ISAR Applications

This section focuses on the application of CS to the ISAR imaging problem. In particular, Sec.III-A deals with the image reconstruction from compressed data, Sec.III-B deals with the problem of resolution enhancement via CS exploitation and Sec.III-C deals with the CS image reconstruction from gapped data.

### A. *Image reconstruction from compressed data*

ISAR signals usually consist of huge matrices of data which determine the computational burden of the image processing. In order to reduce the computational load, a data reduction can be performed. By the way, as the data compression increases, the quality of ISAR images obtained via conventional Fourier based methods decreases. In particular, when the sample structure of the data does not meet the Nyquist's requirement, the ISAR image suffers from high sidelobes and distortion. In this scenario, the capabilities of CS of reconstructing the ISAR image from a compressed signal, which has a number of samples that is lower than the Nyquist bound, is fundamental [3]. CS can be applied in the delay time/frequency dimension, Doppler/slow time dimension or both frequency/slow-time. Without loss of generality, we will focus our attention on the 2D formulation [24]. The advantages of the 2D fomulation in Eq.(19) with respect to 1D methods or staking operations that can be found in literature is that this formulation deals with smaller matrices and so a reduced computational burden [26]. The key concept of the data compression in the CS framework is illustrated in Fig.3(a), in which the data before and after the sensing operation and the ISAR image are schematically represented. As can be easily noticed, the data after the sensing operation is obtained by randomically discarding some samples in the frequency/slow time domain.

### B. *Resolution enhancement*

It is well known that the spatial resolution in ISAR images is strictly related to the transmitted bandwidth and the observation time. In some cases, it may happen that these two parameters are not large enough to obtain a desired range/cross range resolution. Different techniques have been proposed in literature to enhance the resolution of ISAR images, such as spatially variant apodization techniques and bandwidth extrapolation based methods [22][32][39][28]. By the way, these techniques are efficient when the gaps to be filled are small with respect to the whole

spectral and observation time occupancy of the signal. Conversely, CS can be successfully applied to a version of the received signal in which the dimensions in the frequency and slow time domain have been increased, as schematically represented in Fig.3(b). In this case, the available samples are assumed to be the result of a sensing operation performed over a larger domain and the signal is reconstructed over a larger bandwidth and a longer observation time, which leads to a finer resolution.

### C. Image reconstruction from gapped data

A gapped data is defined as an incomplete set of data, in which a large amount of samples are missing in the frequency domain, slow time domain or both. Gaps in the frequency domain can be associated with transmission in non-adjacent frequency ranges, for example in the case in which some bandwidths are dedicated to other services, or in the case of passive radars which exploit the DVB-T signals. A data with gaps in the slow time domain can be associated to the signal acquired by a multi-target radar system, in which different targets are illuminated for different time intervals. A schematic representation of the concept of gapped data is in Fig.3(c). The difference between a compressed data and a gapped data is that in a compressed data the missing samples in a domain are usually associated with very small gaps, which can be the results of a system malfunctioning. In a gapped data, the missing samples correspond to large gaps that can be associated with transmission disruption in frequency or slow time.

### IV. DATASET DESCRIPTION

The proposed CS ISAR image reconstruction algorithm was tested on real data. In particular, two different sets of real data have been used, one acquired by an active system and one by a passive system.

### A. Dataset 1

The data from the active radar consists of a real turntable data publicly released by the Georgia Technology Research Institute (GTRS) [15]. The data contains the phase history of a T72 tank measured for a set of azimuth and elevation angles by a full-polarimetric X band radar. In order to test the algorithm, the data acquired with an azimuth angle and elevation angle equal to of $\theta_{az} = 90$ and $\theta_{el} = 30$ respectively is considered.
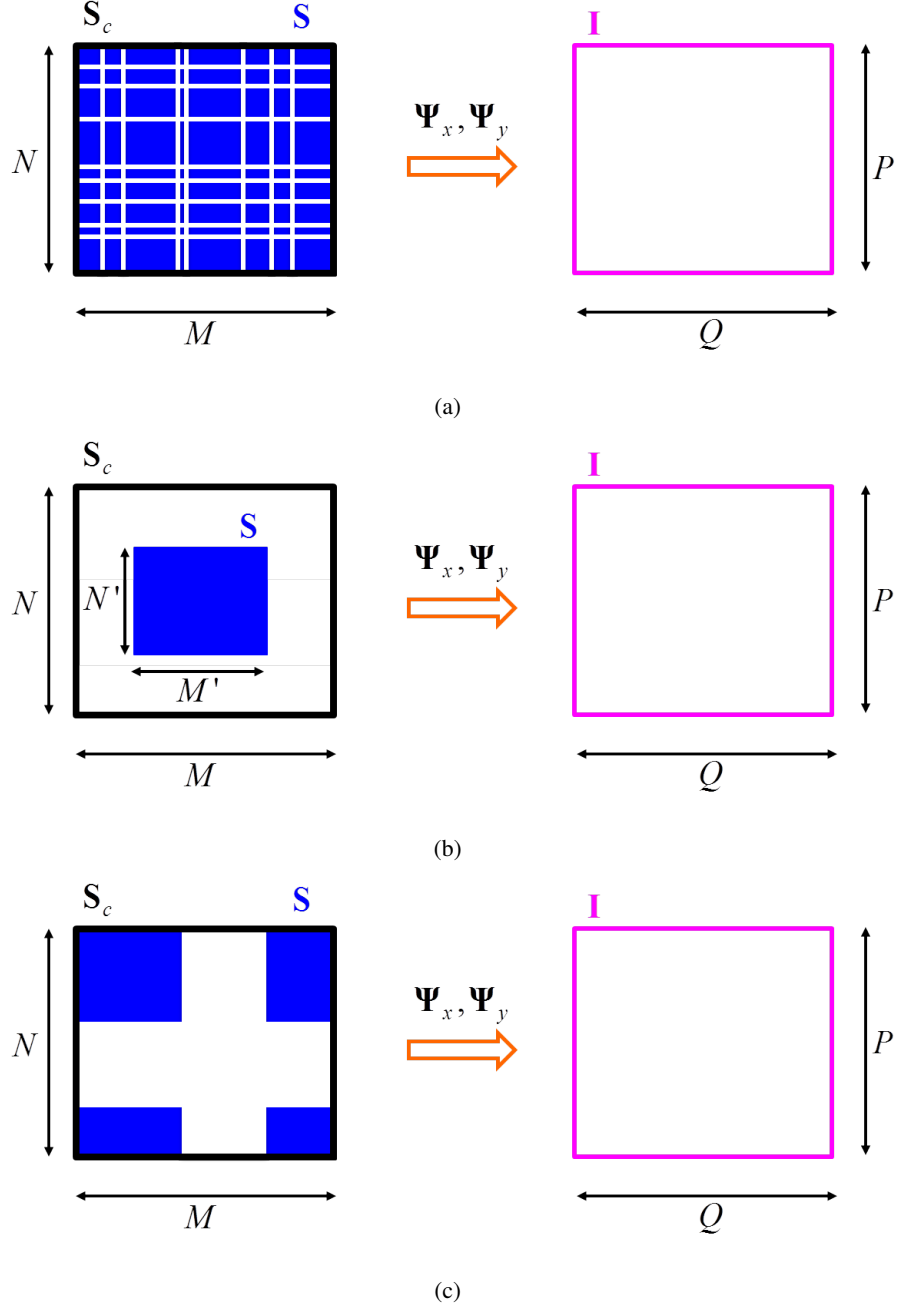
Figure 3. CS data compression (a), resolution enhancement (b) and reconstruction from gapped data (c) concept
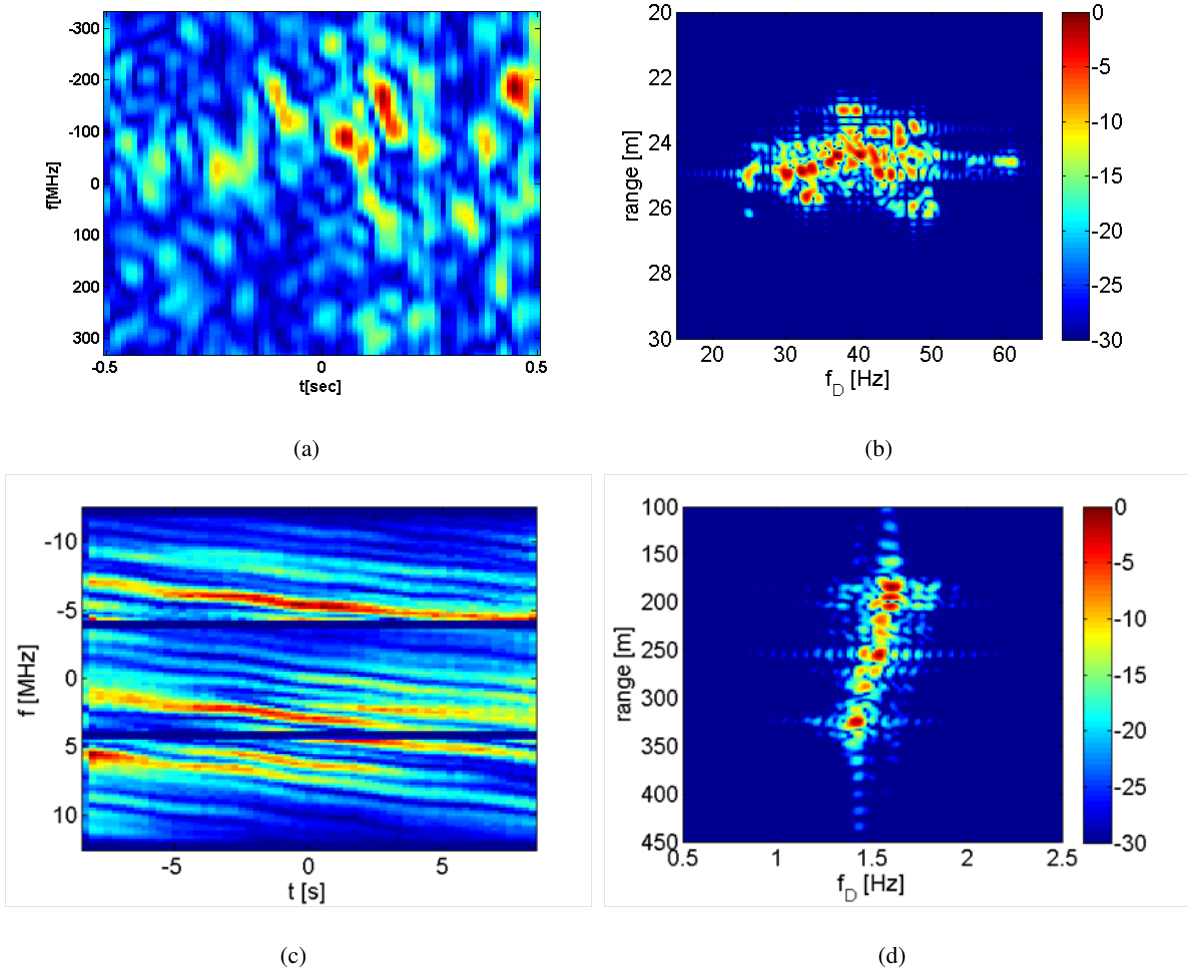
Figure 4.  Real active data (a) and RD image (b). Real passive data (c) and RD image (d)

Fig.4(a) shows the original complete data while Fig.4(b) shows the RD image obtained from the complete data.

## B.  Dataset 2

The real passive data refers to the measurement campaign held in Livorno (Tuscany, Italy) in which a DVB-T passive radar demonstrator developed by the RaSS (Radar and Surveillance System) laboratory team has been employed. The details of this system can be found in [21]. The acquisition geometry is in Fig.4(c). The ISAR data consists of 3 adjacent DVB-T channels, as shown in Fig.4(d).

## V. RESULTS

In this section, the results of the ISAR image reconstruction via CS will be shown and compared to the image obtained via conventional RD algorithm. In order to make a fair comparison, the Image Contrast (IC) [19] is used as a quality index. The image contrast is defined as the ratio between the image intensity standard deviation and the image intensity mean value, as follows

$$IC = \frac{\sqrt{E\{[|\mathbf{I}| - E\{|\mathbf{I}|\}]^2\}}}{E\{|\mathbf{I}|\}} \tag{23}$$

where $E\{\cdot\}$ denotes the expectation over the spatial coordinates of the image and $|I|$ denotes the image intensity. In order to understand the capabilities of the proposed CS ISAR image reconstruction algorithm, the performance will be evaluated in different scenarios. In particular, the IC will be evaluated for different percentages of discarded samples, which will be denoted by compression rate (CR) in all the above mentioned applications, for different SNR (Signal to Noise Ratio) values. It is worth pointing out that each original data contains a noise contribution. For this reason, in order to vary the SNR, a realization of additive Gaussian noise is added to the data so that the SNR can be defined as

$$SNR = \frac{Ps}{P_n + \sigma_n^2} \tag{24}$$

where $P_s$ and $P_n$ denote the useful signal power and the noise power of the original data, respectively, and $\sigma_n^2$ is the standard deviation of the additive Gaussian white noise, which is evaluated by inverting Eq.(24). $P_s$ can be estimated by considering the image obtained by the RD algorithm. In fact, since 2D Fourier transform in the RD algorithm performs a matched filter, the useful signal samples will add coherently in the spatial resolution cells occupied by the target, so that $P_s$ can be estimated as

$$P_s = \frac{1}{P_T Q_T} \sum_{p=1}^{P_T} \sum_{q=1}^{Q_T} |\mathbf{I}(p,q)|^2 \tag{25}$$

where $P_T$ and $Q_T$ denote the resolution cells in Doppler and range occupied by the target. On the other hand, the noise power will be estimated as

$$P_n = \frac{1}{PQ} \sum_{p=1}^{P} \sum_{q=1}^{Q} |\mathbf{I}(p,q)|^2 - P_s \tag{26}$$

*A. Image Reconstruction from compressed data*

Let consider the data of the active system described in Sec.IV-B and suppose to randomly discard samples both in the frequency and in the slow time domain in order to obtain a compressed data, as shown in Fig.5(a). The ratio between the number of discarded samples and the total number of samples denotes the CR in this application. It this case, a $CR = 76\%$ and an $SNR = 5dB$ are used. Fig.5(a)-(b) show the compressed data and ISAR image obtained by applying the RD algorithm to the compressed data respectively. As can be noticed, the ISAR image in Fig.5(b) is highly distorted because of the lack of samples in the compressed data. Conversely, by applying the proposed CS ISAR reconstruction algorithm a good quality image can be obtained, as shown in Fig.5(c). As can be noted from a visual inspection, the distortion effect and the sidelobes are dramatically reduced in the image obtained via the CS ISAR processing and the quality of the image can be compared with that of image obtained via conventional RD algorithm applied to the complete data in Fig.4(b). In addition, the IC plots in Fig.6 show that the image quality does not decrease for a given $SNR$ as the $CR$ increases. However, by observing the plots in Fig.6(a) it can be easily noticed that the IC increases for very high CR values, leading to misleading conclusion on the image quality. In fact, as the CR increases, the number of reconstructed scatterers decreases and the IC increases with respect to the value obtained when more target scatterers are reconstructed. In fact, there exists a relationship between the number of measurements $M'$ and $N'$ and the sparsity degree. Since the sparsity degree of an ISAR image is related to the number of scatterers composing the target, the fewer the measurements, the higher the CR, the fewer the scatterers the CS algorithm effectively reconstructs, so leading to higher IC values.

Similar conclusions can be drawn when observing the results obtained with the passive data in Fig.7. The images in Fig.7 have been obtained by applying the same $CR$ and $SNR$ of the previous case. The comparison between the ISAR image obtained by applying the conventional RD algorithm to the compressed data (Fig.7(b)) and the image obtained with the CS ISAR algorithm (Fig.7(c)) shows a significant enhancement in the image quality. In particular, a comparison between the CS ISAR image and the image obtained with the complete data in Fig.4(d) shows the reconstruction capabilities of the proposed CS-based ISAR algorithm. The performances

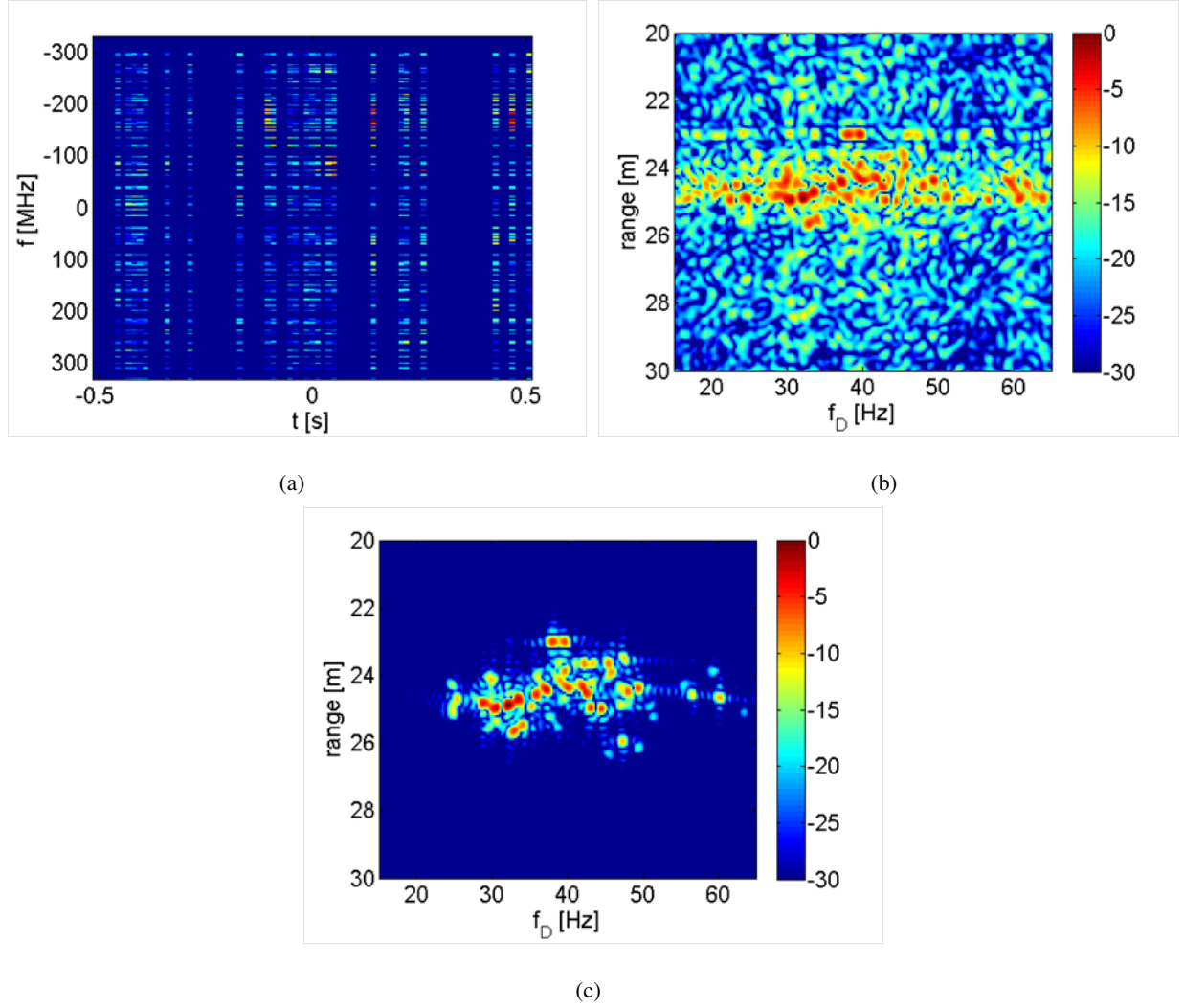(a)                                    (b)



(c)

Figure 5.  ISAR data after compression with $CR = 76\%$ (a), RD image (b) and CS ISAR image (c)

measured by means of the IC show that the RD algorithm reconstruction capabilities decrease as the $CR$ increases. Conversely, the image quality is almost constant for a given $SNR$ as the $CR$ increases for the proposed CS ISAR algorithm. Even in this case, the IC increase for high $CR$ values in the CS ISAR case does not denote an enhancement in the image quality, but a reduced number of reconstructed scatterers.

## B.  Resolution enhancement

As mentioned in Sec.III-B, this application is based on the processing of a version of the acquired data with more samples in both the frequency and in the slow time domain in order to
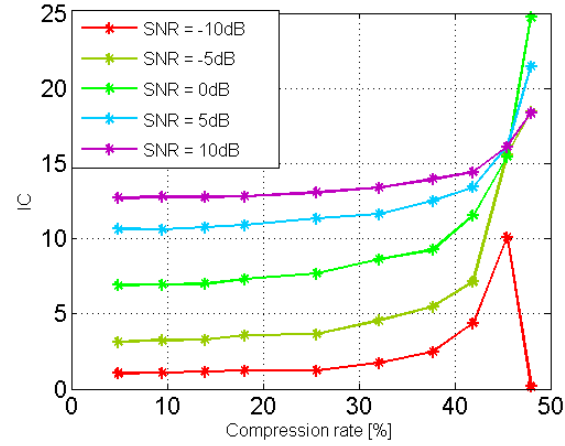
(a)
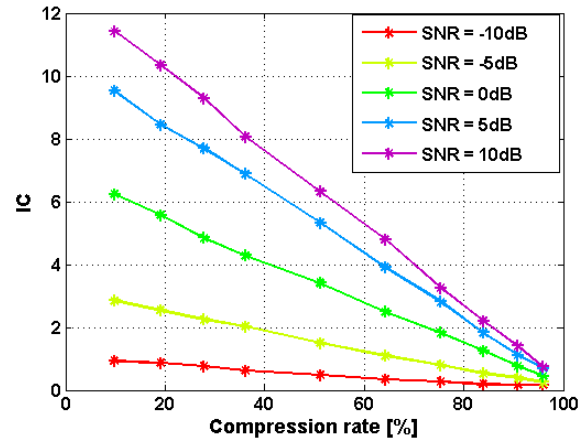


(b)

Figure 6.  IC evaluated for different SNR values in the case of CS ISAR image reconstruction algorithm (a) and conventional RD algorithm (b)

synthesize a larger bandwidth and observation time and, hence, a finer resolution.

In order to clearly understand the reconstruction capabilities in terms of resolution enhancement, the original data sets in Fig.4(a) and Fig.4(c) are taken as touchstones while the acquired data at the input of the processing chain is extracted from the complete one considering a subset of samples in the frequency and slow time domain. For the sake of simplicity, we will refer to the $CR$ also in this case to denote the amount of discarded data with respect to the number of samples in the complete data.

In the case of real active data, the acquired signal is in Fig.9(a) and the amount of discarded
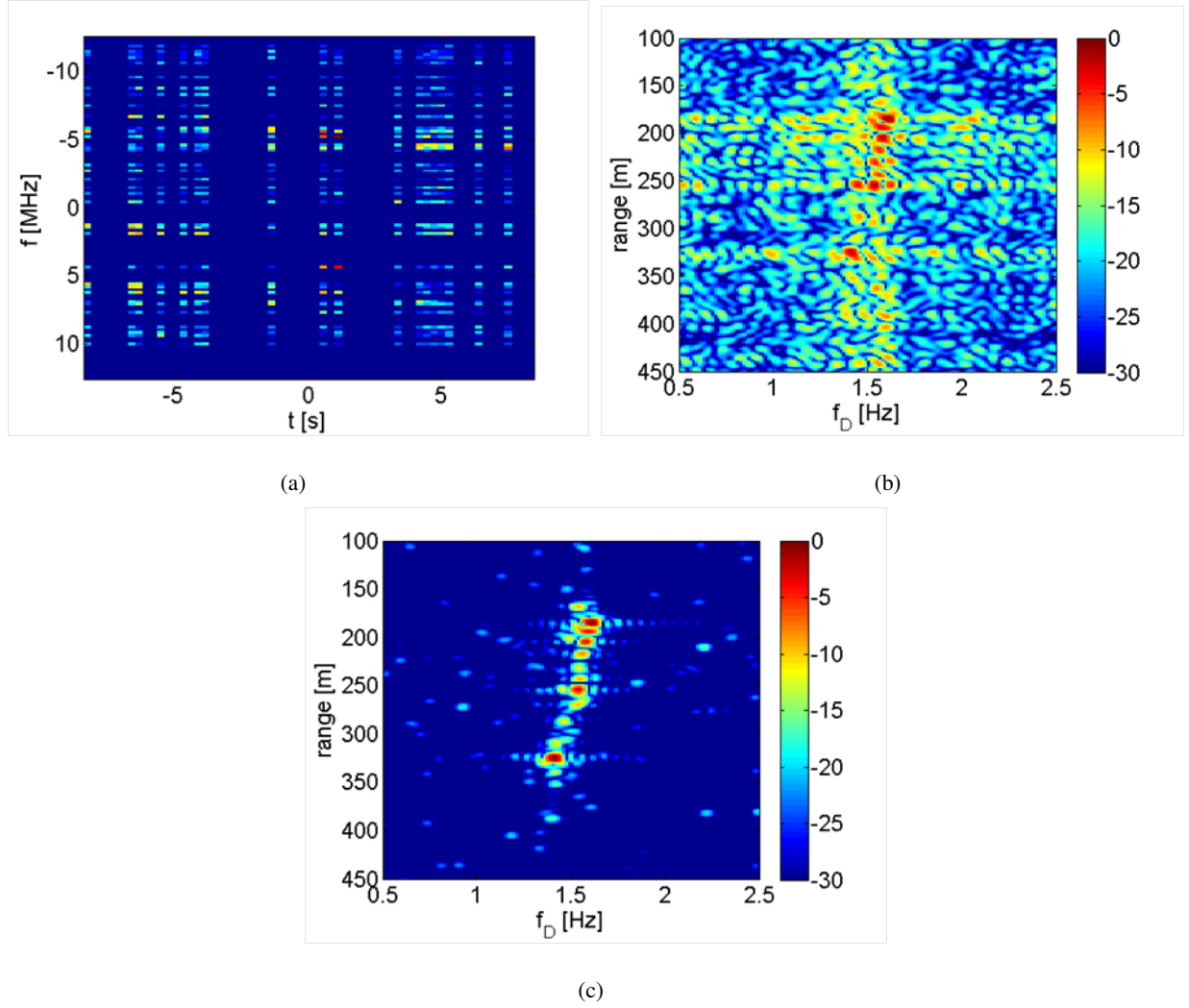
(a)

(b)

(c)

Figure 7. ISAR data after sensing with $CR = 76\%$ (a), RD image (b) and CS ISAR image (c)

data is $50\%$. Fig.9(b) and (c) show the RD image and the CS ISAR image respectively. The image obtained with the CS ISAR algorithm clearly shows a considerable better quality with respect to the RD image. In addition, the quality of the CS ISAR image is comparable with that of the original ISAR image in Fig.4(b). As expected, the performance evaluation by means of IC shows that the image quality decreases as the amount of discarded data increases for the RD algorithm. Conversely, the image quality is almost constant for the CS ISAR image as the CR increases. Even in this scenario, the IC value increase for high CR values is due to some missing scatterers in the reconstructed image with respect to lower CR values.
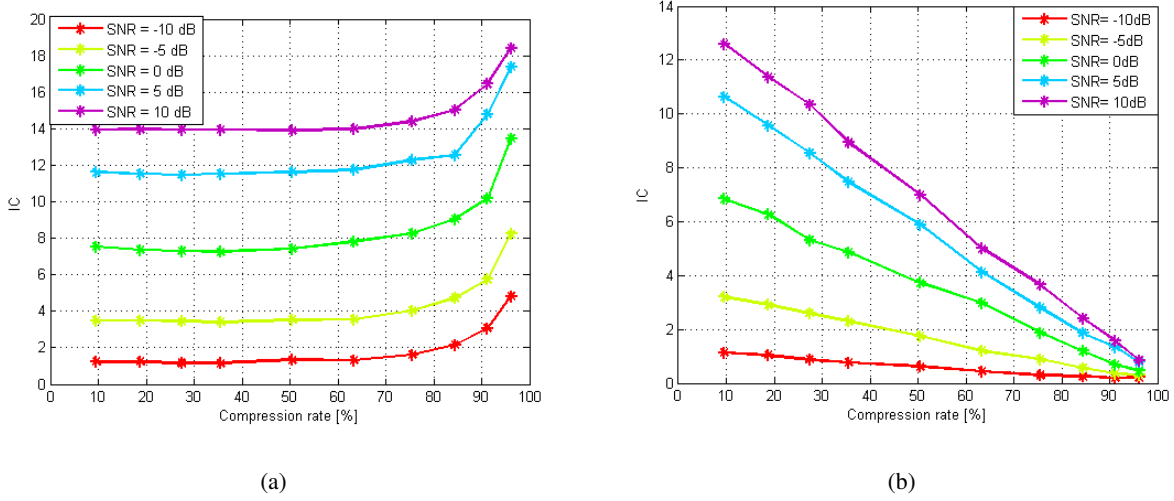
Figure 8. IC evaluated for different SNR values in the case of CS ISAR image reconstruction algorithm (a) and conventional RD algorithm (b)

In the case of passive data, the acquired signal is extracted from the complete one by taking only the central DVB-T channel, as shown in Fig.11(a). In this way, the acquired data has the same number of samples in the slow time domain with respect to the original data, so that the resolution enhancement is expected only in the range domain. The RD image is shown in Fig.11(b) while the CS ISAR image is in Fig.11(c). A visual inspection clearly shows that the distortion effect and the sidelobes are significantly reduced in the CS ISAR image with respect to the RD image. In addition, the IC plots in Fig.11(d) show the CS ISAR algorithm outperforms the RD algorithm for different SNR values.

## C. Image Reconstruction from gapped data

Let consider the dataset associated with the real active system described in Sec.IV-B. A gapped data both in the frequency and slow time domain is extracted from the complete data by discarding samples in the signal domain, as shown in Fig.12(a). The amount of discarded samples is of $70\%$ with respect to the total samples in the complete data. Fig.12(b) and (c) show the RD and the CS ISAR image respectively. The RD image clearly shows high sidelobes while the CS ISAR image is comparable with the RD image obtained from the complete data. As for the previous cases, the IC plots in Fig.13 shows that the image quality is almost constant as the CR increases while the IC decreases for the RD image. The increase in the IC values for high
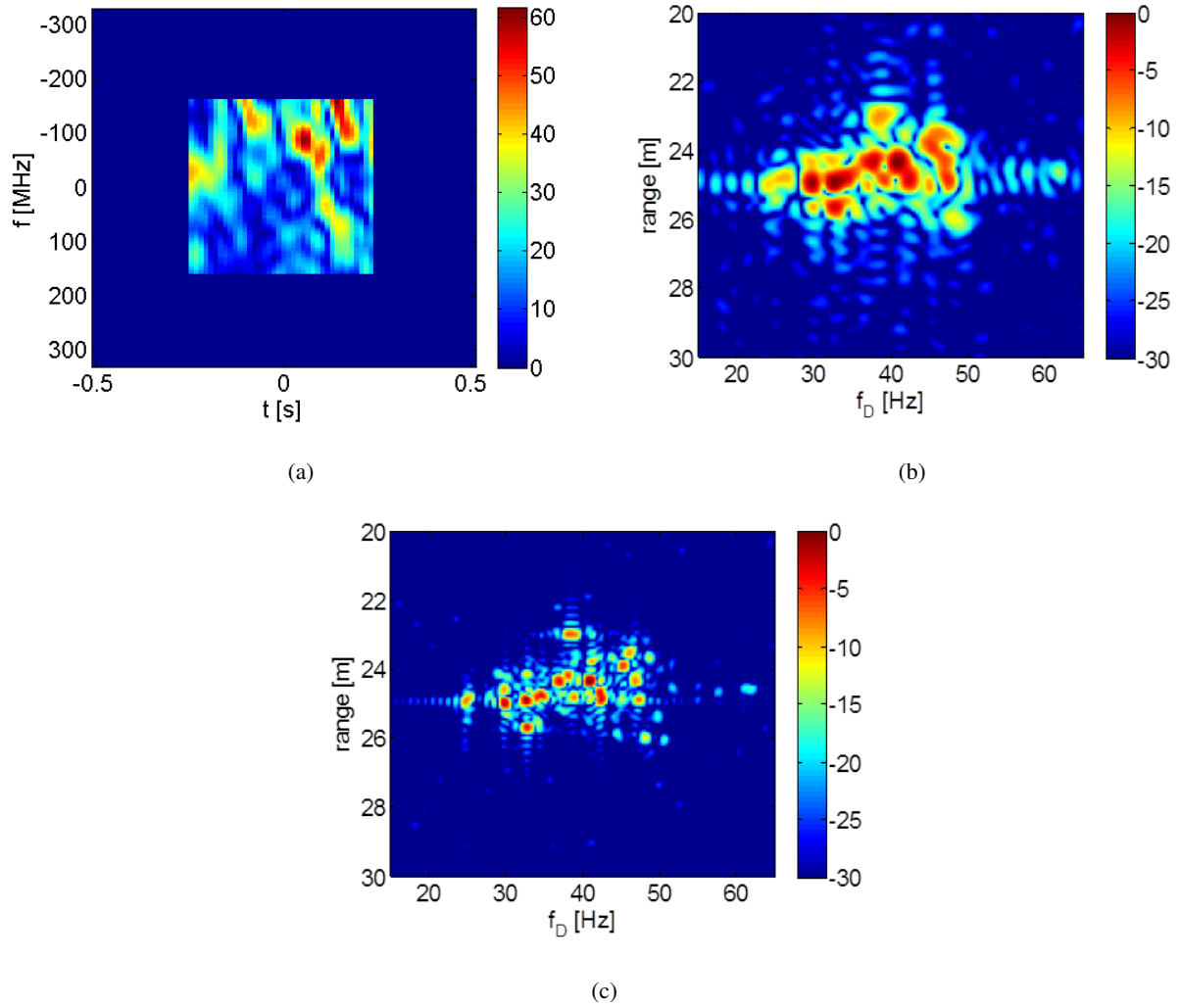
Figure 9. ISAR data after sensing with $CR = 50\%$ (a), RD image (b) and CS ISAR image (c)

CR is compatible with a reduced number of reconstructed scatterers with respect to the case with lower CR.

In the case of passive data, the acquired data is extracted from the complete one by discarding the central DVB-T channel, as shown in Fig.14(a). The RD image and the CS ISAR image are shown in Fig.14(b) and (c) respectively. Even in this scenario, the proposed CS ISAR method outperforms the RD algorithm. This results is also proven by the plots in Fig.14(d), in which the IC for the RD and the CS ISAR image are plotted for different SNR values. These results demonstrate the effectiveness of the CS ISAR algorithm in case of data acquired on non adjacent DVB-T channels.
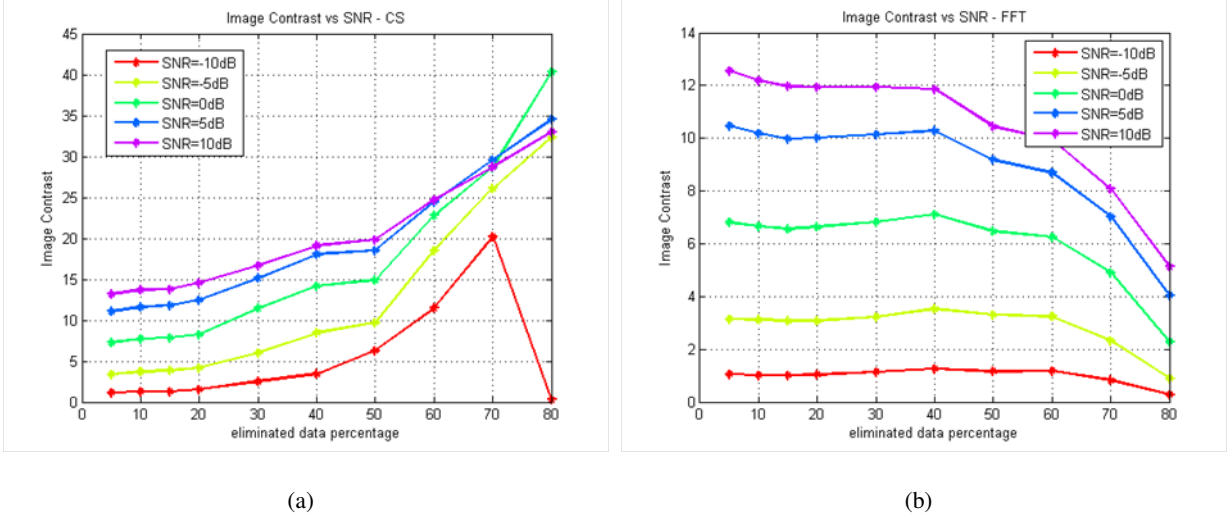
Figure 10. IC evaluated for different SNR values in the case of CS ISAR image reconstruction algorithm (a) and conventional RD algorithm (b)

## VI. Conclusion

In this paper the capabilities of CS for ISAR image reconstruction and resolution enhancement have been demonstrated. In particular, a CS- based ISAR method based on the application of the RD processing to the signal obtained from the CS estimated image has been proposed. This method allows for a fair comparison between the ISAR image obtained via conventional RD processing and the image obtained with the CS-based ISAR method. The proposed method has been applied to two different real datasets to demonstrate the effectiveness of the proposed method in the case of data compression, resolution enhancement and for image reconstruction from gapped data. The comparison between conventional RD processing and the proposed method has been carried out in terms of IC, which has demonstrated the effectiveness of CS ISAR with respect to conventional RD imaging for all the considered applications.

## Acknowledgement
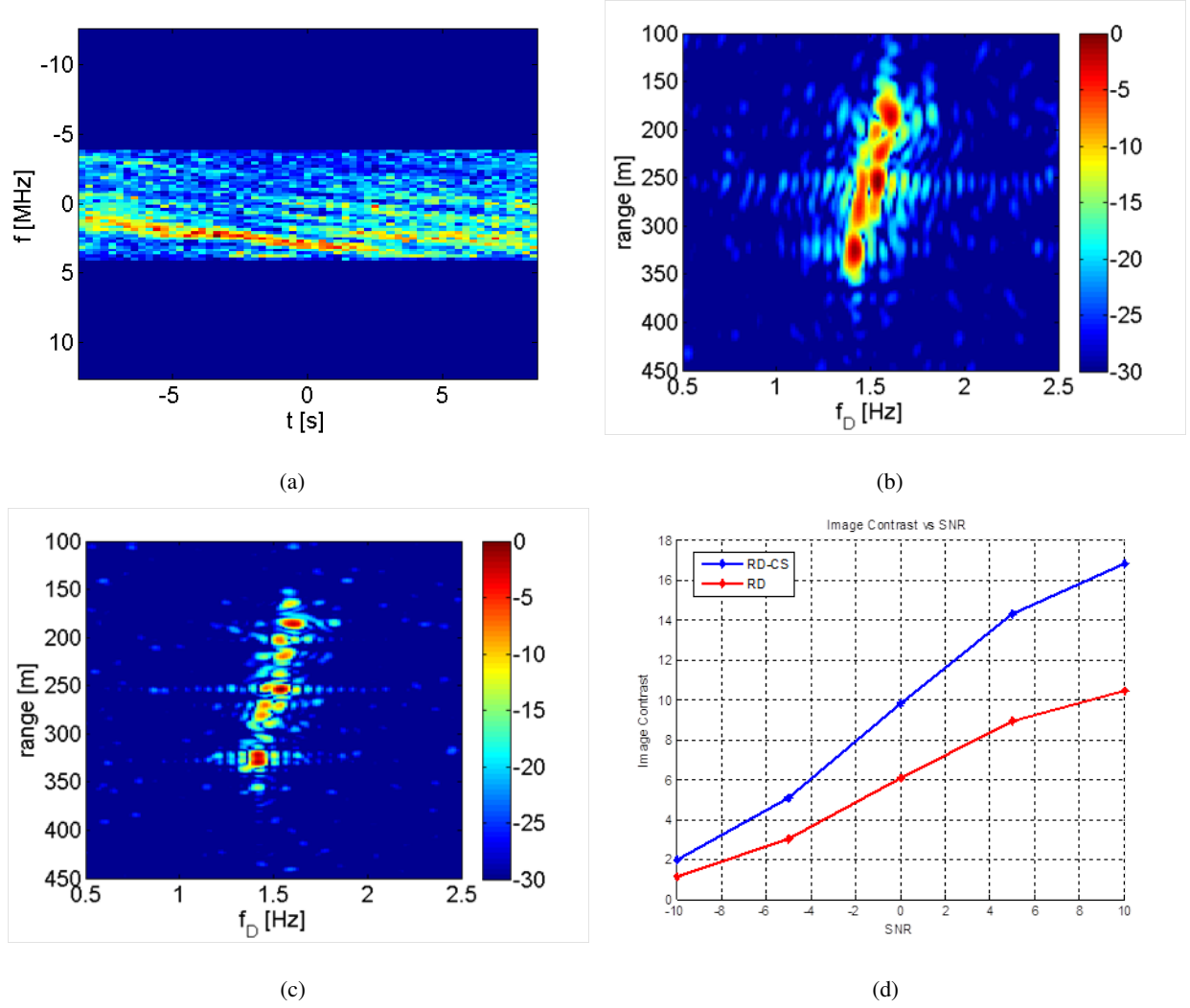
(a)

(b)

(c)

(d)

Figure 11. ISAR data after sensing (a), RD image (b), CS ISAR image (c) and IC (d)

## REFERENCES

[1] A. Bacci, E. Giusti, S. Tomei, M. Martorella, and F. Berizzi. Time-slotted FMCW MIMO ISAR with compressive sensing image reconstruction. In *3rd International Workshop on Compressive Sensing applied to Radar (CoSeRa2015)*, Sept 2013.

[2] R. Baraniuk and P. Steeghs. Compressive radar imaging. In *Radar Conference, 2007 IEEE*, pages 128–133, April 2007.

[3] B.C.Zhang, W. Hong, and Y. Wu. Sparse microwave imaging: Principles and applications. *Science China*, 55(8):1722–1754, August 2012.

[4] F. Berizzi, E. Dalle Mese, and M. Martorella. ISAR imaging of oscillating targets by range-instantaneous-Doppler technique. In *Radar Conference, 2000. The Record of the IEEE 2000 International*, pages 475–480, 2000.

[5] V.C. Chen and M. Martorella. *Inverse Synthetic Aperture Radar Imaging; Principles, Algorithms and Applications*. Institution of Engineering and Technology, 2014.
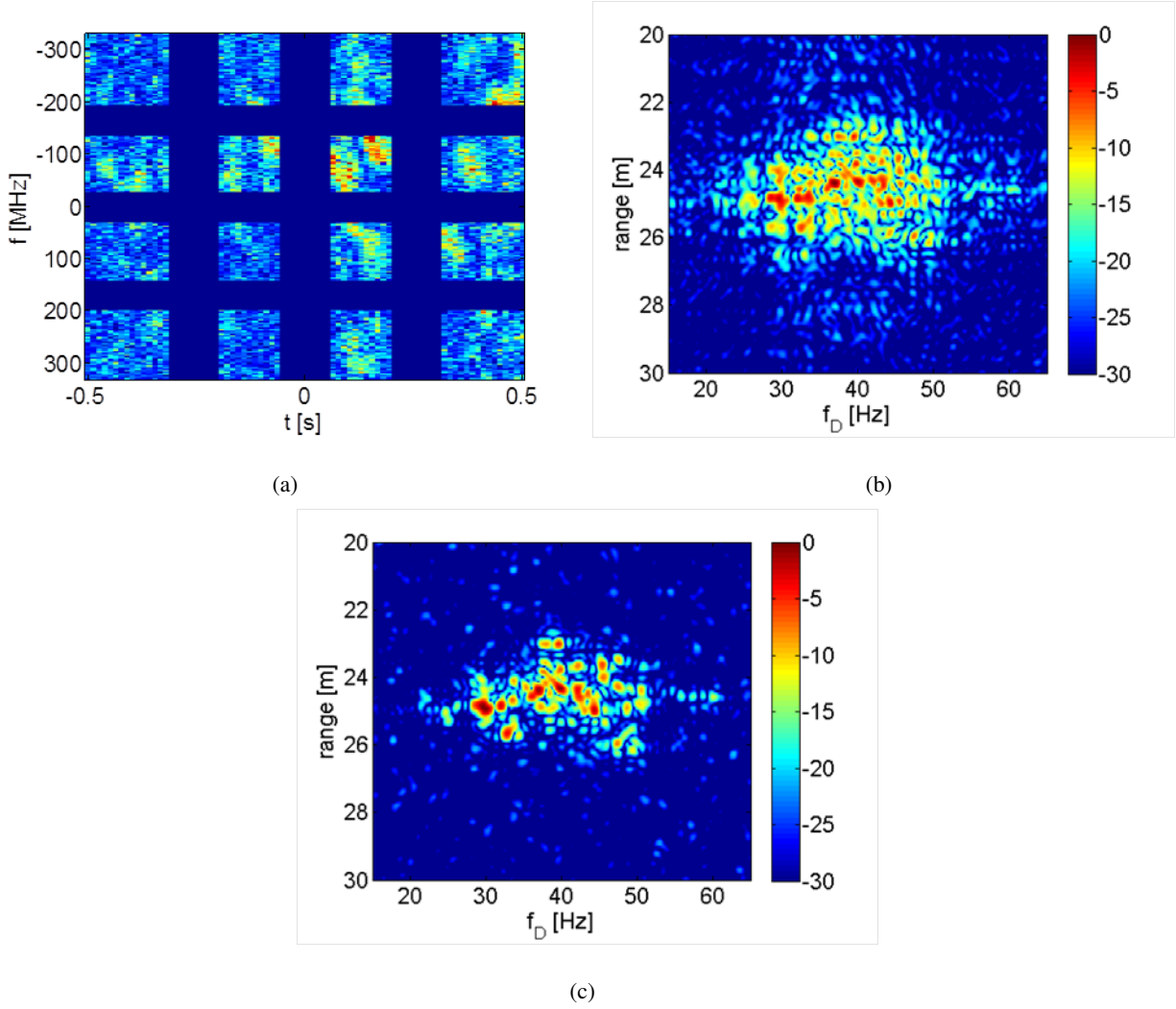
(a)

(b)



(c)

Figure 12. ISAR data after sensing with $CR = 76\%$ (a), RD image (b) and CS ISAR image (c)

[6] Ping Cheng, Haitian Liu, and Zhongkai Zhao. A compressive sensing-based technique for ISAR imaging. In *Millimeter Waves (GSMM), 2012 5th Global Symposium on*, pages 466–469, May 2012.

[7] H. Chinmay, R. Baraniuk, M. A. Davenport, and M. F. Duarte. *An Introduction to Compressive Sensing*. OpenStax CNX., 27 August 2014.

[8] Can Feng, Liang Xiao, and Zhihui Wei. Compressive sensing ISAR imaging with stepped frequency continuous wave via gini sparsity. In *Geoscience and Remote Sensing Symposium (IGARSS), 2013 IEEE International*, pages 2063–2066, July 2013.

[9] A. Ghaffari, M. Babaie-Zadeh, and C. Jutten. Sparse decomposition of two dimensional signals. In *Acoustics, Speech and Signal Processing, 2009. ICASSP 2009. IEEE International Conference on*, pages 3157–3160, 2009.

[10] E. Giusti, A. Bacci, S. Tomei, and M. Martorella. Compressive sensing based ISAR: Performance Evaluation. In *Radar Symposium (IRS), 2015 16th International*, June 2015.
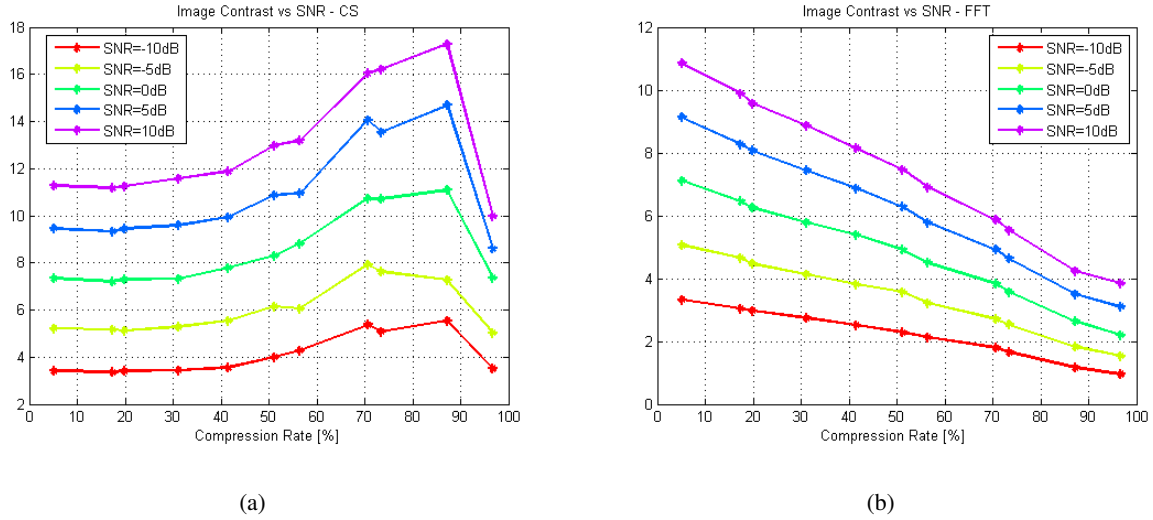
(a)            (b)

Figure 13. IC evaluated for different SNR values in the case of CS ISAR image reconstruction algorithm (a) and conventional RD algorithm (b)

[11] E. Giusti, S. Tomei, A. Bacci, M. Martorella, and F. Berizzi. Autofocus for CS based ISAR imaging in the presence of gapped data. In *2nd International Workshop on Compressive Sensing applied to Radar (CoSeRa2013)*, Sept 2013.

[12] Elisa Giusti, Qiu Wei, Alessio Bacci, Sonia Tomei, and Marco Martorella. Super resolution ISAR imaging via compressing sensing. In *EUSAR 2014; 10th European Conference on Synthetic Aperture Radar; Proceedings of*, pages 1–4, June 2014.

[13] S.K. Gunnala, L.M. Camacho, and S. Tjuatja. Target detection above rough surfaces in microwave imaging using compressive sampling. In *Geoscience and Remote Sensing Symposium (IGARSS), 2010 IEEE International*, pages 3498–3501, July 2010.

[14] Ali Cafer Gurbuz, J.H. McClellan, and W.R. Scott. Compressive sensing for gpr imaging. In *Signals, Systems and Computers, 2007. ACSSC 2007. Conference Record of the Forty-First Asilomar Conference on*, pages 2223–2227, Nov 2007.

[15] https://www.sdms.afrl.af.mil/.

[16] Huang Lu and Zhang Qianqian. 2D ISAR imaging scheme in complex baseband echo domain based on compressive sensing. In *Information and Communications Technologies (ICT 2014), 2014 International Conference on*, pages 1–5, May 2014.

[17] M. Lustig, D.L. Donoho, J.M. Santos, and J.M. Pauly. Compressed sensing MRI. *Signal Processing Magazine, IEEE*, 25(2):72–82, March 2008.

[18] M. Martorella. Novel approach for isar image cross-range scaling. *Aerospace and Electronic Systems, IEEE Transactions on*, 44(1):281–294, January 2008.

[19] M. Martorella, F. Berizzi, and B. Haywood. Contrast maximisation based technique for 2-D ISAR autofocusing. *Radar, Sonar and Navigation, IEE Proceedings -*, 152(4):253–262, Aug 2005.

[20] M. Martorella, J. Palmer, J. Homer, B. Littleton, and I.D. Longstaff. On bistatic inverse synthetic aperture radar. *Aerospace and Electronic Systems, IEEE Transactions on*, 43(3):1125–1134, 2007.

[21] D. Olivadese, E. Giusti, D. Petri, M. Martorella, A. Capria, and F. Berizzi. Passive ISAR with DVB-T signals. *Geoscience*
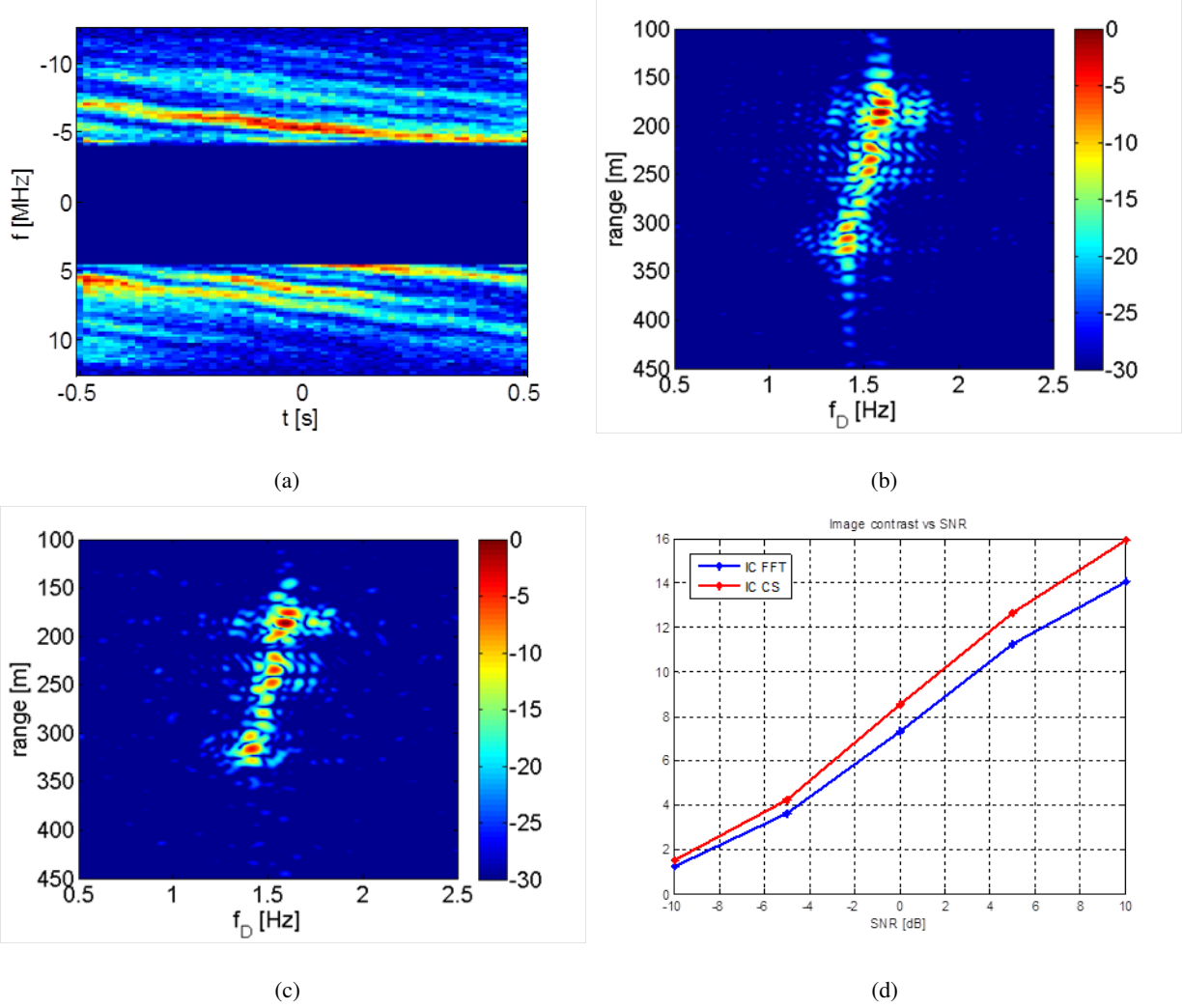
Figure 14. ISAR data after sensing (a), RD image (b) and CS ISAR image (c)

*and Remote Sensing, IEEE Transactions on*, 51(8):4508–4517, Aug 2013.

[22] D. Olivadese, M. Martorella, and F. Berizzi. Multi-channel P-ISAR grating lobes cancellation. In *Radar Systems (Radar 2012), IET International Conference on*, pages 1–5, Oct 2012.

[23] D. Petri, C. Moscardini, M. Martorella, M. Conti, A. Capria, and F. Berizzi. Performance analysis of the batches algorithm for range-doppler map formation in passive bistatic radar. In *Radar Systems (Radar 2012), IET International Conference on*, pages 1–4, Oct 2012.

[24] W. Qiu, E. Giusti, A. Bacci, M. Martorella, F. Berizzi, H.Z. Zhao, and Q. Fu. Compressive sensing for passive ISAR with DVB-T signal. In *Radar Symposium (IRS), 2013 14th International*, volume 1, pages 113–118, June 2013.

[25] Wei Qiu, M. Martorella, Jianxiong Zhou, Hongzhong Zhao, and Qiang Fu. Three-dimensional inverse synthetic aperture radar imaging based on compressive sensing. *Radar, Sonar Navigation, IET*, 9(4):411–420, 2015.

[26] Wei Qiu, Hongzhong Zhao, Jianxiong Zhou, and Qiang Fu. High-resolution fully polarimetric ISAR imaging based on

compressive sensing. *Geoscience and Remote Sensing, IEEE Transactions on*, 52(10):6119–6131, Oct 2014.

[27] R.G. Raj, R. Lipps, and A.M. Bottoms. Sparsity-based image reconstruction techniques for ISAR imaging. In *Radar Conference, 2014 IEEE*, pages 0974–0979, May 2014.

[28] G. Thomas and N. Gadhok. Sidelobe apodization in fourier imaging. In *Signals, Systems and Computers, 2001. Conference Record of the Thirty-Fifth Asilomar Conference on*, volume 2, pages 1369–1373 vol.2, Nov 2001.

[29] Hongxian Wang, Yinghui Quan, Mengdao Xing, and Shouhong Zhang. ISAR imaging via sparse probing frequencies. *Geoscience and Remote Sensing Letters, IEEE*, 8(3):451–455, May 2011.

[30] Yong Wang, Jian Kang, and Runbin Zhang. ISAR imaging with random missing observations based on non-iterative signal reconstruction algorithm. In *Signal Processing (ICSP), 2014 12th International Conference on*, pages 1876–1879, Oct 2014.

[31] D.R. Wehner. *High resolution radar*. Artech House radar library. Artech House, 1987.

[32] Xiaojian Xu and R.M. Narayanan. Enhanced resolution in SAR/ISARimaging using iterative sidelobe apodization. *Image Processing, IEEE Transactions on*, 14(4):537–547, April 2005.

[33] Yao Yu, A.P. Petropulu, and H.V. Poor. Mimo radar using compressive sampling. *Selected Topics in Signal Processing, IEEE Journal of*, 4(1):146–163, Feb 2010.

[34] Lei Zhang, Zhi Jun Qiao, Meng Dao Xing, Jian Lian Sheng, Rui Guo, and Zheng Bao. High-resolution ISAR imaging by exploiting sparse apertures. *Antennas and Propagation, IEEE Transactions on*, 60(2):997–1008, 2012.

[35] Lei Zhang, Zhi-Jun Qiao, Mengdao Xing, Yachao Li, and Zheng Bao. High-resolution ISAR imaging with sparse stepped-frequency waveforms. *Geoscience and Remote Sensing, IEEE Transactions on*, 49(11):4630–4651, 2011.

[36] Lei Zhang, Mengdao Xing, Cheng-Wei Qiu, Jun Li, Jialian Sheng, Yachao Li, and Zheng Bao. Resolution enhancement for Inversed Synthetic Aperture Radar imaging under low snr via improved compressive sensing. *Geoscience and Remote Sensing, IEEE Transactions on*, 48(10):3824–3838, 2010.

[37] F. Zhu, Q. Zhang, Y. Xiang, and Y.Q. Feng. Compressive sensing in ISAR spectrogram data transmission. In *Synthetic Aperture Radar, 2009. APSAR 2009. 2nd Asian-Pacific Conference on*, pages 89–92, Oct 2009.

[38] F. Zhu, Q. Zhang, J.B. Yan, F.F. Gu, and S. Liu. Compressed sensing in ISAR imaging with sparse sub-aperture. In *Radar (Radar), 2011 IEEE CIE International Conference on*, volume 2, pages 1463–1466, Oct 2011.

[39] Long Zhuang, Xingzhao Liu, and Zhixin Zhou. Enhanced resolution for sparse aperture radar imaging using super-SVA. In *Microwave Conference, 2007. APMC 2007. Asia-Pacific*, pages 1–4, Dec 2007.